

# AsyMov: Integrated Sensing and Communications with Asynchronous Moving Devices

Gianmaria Ventura<sup>†</sup>, Graduate Student Member, IEEE, Zaman Bhalli<sup>†</sup>, Graduate Student Member, IEEE, Michele Rossi<sup>†\*</sup> Senior Member, IEEE, Jacopo Pegoraro<sup>†</sup>, Member, IEEE

**Abstract**—Estimating the Doppler frequency shift caused by moving targets is one of the key objectives of Integrated Sensing And Communication (ISAC) systems. In the case of Wi-Fi sensing, a reliable estimation of the Doppler enables applications such as target classification, human activity recognition, and gait analysis. However, in practical scenarios, Doppler estimation is hindered by the movement of transmitter and receiver devices, and by the phase offsets caused by their clock asynchrony. Existing approaches have separately addressed these two aspects, either assuming clock-synchronous moving devices or asynchronous static ones. Jointly tackling device motion and clock asynchrony is extremely challenging, as the Doppler shift from device movement differs for each propagation path and the phase offsets are time-varying. In this paper, we present AsyMov, a method to estimate the bistatic Doppler frequency of a target and the device velocity in ISAC setups featuring *mobile and asynchronous* devices. Our method leverages the channel impulse response at the receiver, by originally exploiting the invariance of phase offsets across propagation paths and the bistatic geometry. Moreover, AsyMov handles irregular channel sampling in the time domain and can be seamlessly integrated with device velocity measurements obtained from onboard sensors (if available), to enhance its reliability. AsyMov is thoroughly characterized from a theoretical perspective, via numerical simulation, and experimentally, implementing it o

n an IEEE 802.11ay testbed. Numerical and experimental results show superior performance against traditional methods based on the discrete Fourier transform and are on par with similar scenarios featuring static ISAC devices.

**Index Terms**—Integrated sensing and communication, synchronization, Wi-Fi sensing, mobile devices, Doppler frequency.

## I. INTRODUCTION

Integrated Sensing And Communication (ISAC) is expected to be a cornerstone of future wireless communication systems, including next-generation Wi-Fi [1]. One of the key uses of ISAC concerns the estimation of the Doppler frequency caused by a moving target, which also reveals its velocity. On the one hand, Doppler estimation enhances the sensing resolution of the system, as it allows distinguishing targets moving at different speeds [2]. On the other hand, the Doppler effect can be leveraged by a wide range of fine-grained cellular and Wi-Fi sensing applications, such as person identification based on gait [3], fall detection [4], drone monitoring [5], and human movement classification for smart homes and remote healthcare [6], [7].

Compared to indoor radar systems, Doppler estimation in ISAC poses several challenges. First, ISAC transmitter (TX) and receiver (RX) devices are spatially separated (bistatic), so they rely on *asynchronous* Local Oscillators (LOs) to

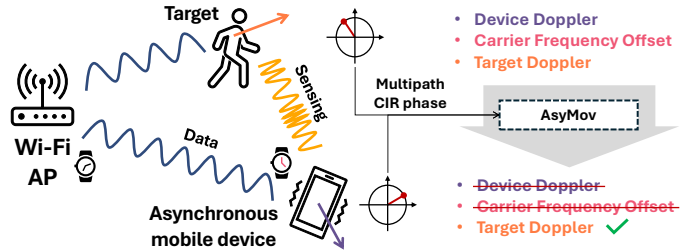


Fig. 1: Overview of AsyMov.

generate the carrier signal, which is consequently affected by a time-varying relative drift [8]. This causes Timing Offset (TO), Carrier Frequency Offset (CFO), and a random Phase Offset (PO) across different transmissions. CFO and PO prevent the coherent processing of channel measurements across time, which is required for the estimation of the Doppler frequency [9]. Second, differently from what is commonly assumed in ISAC research, an *additional* Doppler frequency contribution appears on the reflected signal due to the movement of the TX or RX device. The key challenge in *jointly* addressing clock asynchrony and moving TX/RX devices descends from the different properties of CFO/PO and from the motion-induced Doppler component of the mobile device, which adds up to the Doppler caused by the target. In fact, the noise due to CFO/PO is the same for all propagation paths [10] (spatial domain), but changes across subsequent communication packets (time domain), whereas the device Doppler changes slowly over time but causes a different frequency shift on each propagation path. Existing techniques based on cross-antenna processing, [8], or reference paths, [10], [11], cannot concurrently cope with such spatial and temporal dynamics. Existing solutions only address the following scenarios: (i) *moving* monostatic radar systems, which are not affected by CFO and PO [12]–[14] and only need to compensate for the device Doppler shift, or (ii) asynchronous ISAC systems with *static* devices [9], [10], [15], which are only affected by CFO and PO. Either case poses stringent assumptions to the application scenario, limiting the range of use of previous solutions.

In this work, we propose AsyMov, a method to estimate the Doppler frequency of a target and the device velocity in bistatic mobile ISAC setups using the sole wireless signal. To this end, we leverage the growing trend in next-generation Wi-Fi systems, and in wireless communications in general, of adopting a large communication bandwidth [16]. This yields a good multipath resolution, which can be exploited to extract path-specific signal features.

Our approach obtains phase measurements from different multipath reflections across time in the Channel Impulse

<sup>†</sup>These authors are with the University of Padova, Dept. of Information Engineering. \*This author is with the University of Padova, Dept. of Mathematics. Corresponding author email: jacopo.pegoraro@unipd.it.

Response (CIR). Then, it removes CFO and PO by leveraging their invariance across the received propagation paths. Path-specific phase terms are subsequently removed via time-domain phase differencing, thanks to their slow varying nature over short time windows. Most importantly, each multipath component is *differently* affected by the TX or RX motion, and we exploit this as a source of *diversity* to reduce the number of unknowns in the phase measurements model. As a result, we are able to cast the Doppler frequency estimation of the target as a non-linear system of equations, which can be solved if at least 2 multipath components from static scatterers are available. This means that if the propagation environment has at least two static reflections, the Doppler of the target and the ISAC device velocity can be estimated. To increase the reliability of such estimates, the proposed algorithm refines the solution using subsequent measurements. Differently from traditional Discrete Fourier Transform (DFT)- or Multiple Signal Classification (MUSIC)-based Doppler estimation, AsyMov is robust to *irregular* sampling of the CIR. This means that it can be implemented in ISAC systems with minimal overhead by opportunistically exploiting the transmissions of data packets, and without requiring the transmission of additional signals for sensing or applying sparse channel reconstruction methods [17]. Moreover, AsyMov can seamlessly integrate measurements of the moving device velocity obtained with an onboard Inertial Measurement Unit (IMU), which may be available on mobile devices. We experimentally verify that the onboard IMU is less accurate than our approach based on the sole wireless signal, but increases the Doppler frequency estimation reliability in case fewer than two static multipath components are available.

We conduct an extensive evaluation of AsyMov along two lines. First, we analyze its performance limits by obtaining the Cramér-Rao Lower Bound (CRLB) for the target's Doppler frequency estimation and performing numerical simulations. Second, we evaluate it on real measurements obtained with an IEEE 802.11ay ISAC system in the 60 GHz band. We compare our approach to standard Doppler estimation based on the DFT and to the case where both TX and RX are static.

The contributions of this paper are summarized as follows.

- 1) We solve the problem of estimating the Doppler frequency of a target and the device velocity in bistatic ISAC with asynchronous moving devices. Our solution is solely based on analyzing the received wireless signal, leveraging CIR phase measurements.
- 2) We derive the CRLB for Doppler frequency estimation based on our measurement model and propose a more practical, approximate CRLB expression. Using numerical simulations, we show that AsyMov achieves accurate Doppler frequency estimation with different carrier frequencies and Signal-to-Noise Ratios (SNRs).
- 3) We evaluate the performance of the proposed algorithm on real measurements, collected with a 60 GHz IEEE 802.11ay testbed in different setups. Our results show that AsyMov achieves estimation errors as low as 3 Hz for the Doppler frequency,  $10^\circ$  for device movement direction, and 3 cm/s for the device speed.
- 4) We demonstrate that our approach outperforms standard

methods based on DFT and a benchmark algorithm that estimates the device movement with an onboard IMU sensor. Moreover, we show that AsyMov can easily be integrated with no effort with the IMU measurements when the number of multipath components in the CIR is insufficient, enhancing the estimation reliability.

The paper is organized as follows. In Section II we discuss the related work. We introduce the reference scenario and system model in Section III. AsyMov is presented in Section IV. Section V contains an analysis of AsyMov, with the derivation of the CRLB and the numerical results. Section VI contains experimental results demonstrating the performance of our approach, while concluding remarks are given in Section VII.

## II. RELATED WORK

*Synchronous ISAC.* Monostatic full-duplex technology for ISAC has been investigated in many works. In [18], [19], beamforming, waveform optimization, and phased array architectures have been examined to enable full-duplex ISAC in Millimeter-Wave (mmWave) 5G systems. [17], [20] focused on micro-Doppler spectrogram estimation for indoor human sensing, using a monostatic full-duplex IEEE 802.11ay system. However, full-duplex technology suffers from strong self-interference which remains a challenging and still open issue [18]. As a solution, the transmitted power can be reduced to avoid saturation at the receiver, but this is only feasible in small indoor scenarios and reduces the communication SNR [20]. Other works [21]–[23] have addressed bistatic Doppler estimation through linear methods in mmWave ISAC systems, assuming synchronized static devices.

Since synchronous transceivers are unaffected by CFO and PO, the above works apply standard techniques from time-frequency analysis to obtain the Doppler shift caused by the targets. However, with asynchronous moving devices these methods fail due to the superposition of the phase offsets, the device movement, and the target's Doppler frequency.

*Bistatic asynchronous ISAC.* Existing works on bistatic ISAC which tackled the clock asynchronism between TX and RX can be categorized into two groups.

One group of works exploits the fact that the clock offsets across multiple antennas at the RX are the same due to the shared LO. In [24], the authors propose the Cross-Antenna Cross-Correlation (CACC) method to remove TO and CFO. Similarly, [25]–[27] use the Cross-Antenna Signal Ratio (CASR) method, which removes phase offsets by obtaining the ratio of the channel state information between antennas and enables Doppler estimation. Authors in [26] analyze CASR using the Mobius transform to estimate the Doppler frequency shift with the Long-Range wide area (LoRa) technology. In [27], instead, the multi-person respiration sensing is modeled as a blind source separation problem and efficiently solved by independent component analysis. Cross-antenna methods require multiple antennas at the receiver, which becomes costly at higher frequencies (such as in mmWave systems), where typically phased arrays are preferred. Moreover, they add complexity to the estimation of the sensing parameters by introducing non-linearity.

The second group of works exploits a reference propagation path. [28] proposes a new low-complexity method relying on the correlation between Line-of-Sight (LoS) and Non-Line-of-Sight (NLoS) paths to compensate for the CFO. After the compensation, the Doppler frequency is estimated through DFT. [10] proposes a correlation-based algorithm to compensate for the CFO which is robust to multitarget and NLoS scenarios to compute the micro-Doppler spectrum via a short-time DFT.

The above bistatic ISAC methods all assume *static* TX and RX, which can be a huge limitation in real-world ISAC applications. The device movement introduces an additional Doppler frequency shift which differs for each propagation path and can not be tackled by the mentioned methods.

*Mobile transceiver ISAC.* Existing solutions for wireless sensing with moving devices mostly consider dedicated monostatic mmWave radars. This avoids self-interference, CFO, and PO, and makes the problem significantly simpler. In [12] and [13], the Doppler phase information is extracted by removing the effect of device motion using reflections on background static objects. Recently, the authors of [14] introduced the dynamic Fresnel zone model to link the variation in the received signal and the receiver movement. However, this work does not provide a method to estimate the Doppler frequency of the target and focuses instead on activity recognition.

To the best of our knowledge, the only work addressing ISAC with asynchronous and mobile devices is [29]. This work presents several limitations compared to AsyMov. First, a theoretical analysis of the sensitivity of the Doppler estimation to noise and multipath channel parameters is missing. Moreover, no experimental validation with real measurements is carried out, while we test AsyMov using an IEEE 802.11ay Radio Frequency System on a Chip (RFSoc) ISAC system. Finally, [29] assumes a constant channel estimation period, which is unrealistic in ISAC. Conversely, AsyMov is robust to irregular channel estimation (sampling) times.

### III. MOBILE ISAC SYSTEM MODEL

In this section, we introduce the mobile ISAC system model. This includes the reference scenario, the channel model, and the expressions of the phase measurements.

#### A. Reference scenario

Consider two ISAC devices acting, respectively, as transmitter (TX) and receiver (RX), located on a 2-dimensional (2D), horizontal Cartesian plane. Denote by  $t$  the continuous time variable, and refer to  $\mathbf{x}^{\text{tx}}(t)$  and  $\mathbf{x}^{\text{rx}}(t)$  as the time-varying locations of the TX and RX devices, respectively. In the following, we consider the TX to be mobile, while the RX is static, i.e.,  $\mathbf{x}^{\text{rx}}(t) = \mathbf{x}^{\text{rx}}$ . We call  $v^{\text{tx}}(t)$  and  $\eta(t)$  the TX speed and movement direction with respect to the elongation of the LoS segment between TX and RX. Note that this assumption is not restrictive, since the symmetric case in which the RX moves and the TX is static is analogous, as further discussed in Section III-B, and leads to similar derivations. Note also that our model still holds if the TX and RX are both mobile. In this case, we consider  $v^{\text{tx}}(t)$ ,  $\eta(t)$  to be the *relative* velocity magnitude and the direction between the TX and the RX.

We consider  $Q$  static or mobile scatterers in the environment, indexed by  $q = 1, \dots, Q$ , each at location  $\mathbf{x}_q(t)$ . Mobile scatterers have a velocity  $v_q(t)$  that forms an angle  $\gamma_q(t)$  with the bisector line of the angle formed by the TX, the scatterer, and the RX, denoted by  $\beta_q(t)$  (*bistatic angle*), as shown in Fig. 2. We aim to estimate the bistatic Doppler frequency caused by a moving scatterer of interest, called *target* using channel estimates obtained by the RX as part of normal communication and Angle of Departure (AoD) estimates. In the symmetric case where the RX moves, the AoD would be replaced by the Angle of Arrival (AoA) (see Section III-B).

#### B. Channel model

Consider the wireless signal transmitted by the TX device. We call  $\lambda = c/f_c$  the wavelength of the transmitted signal carrier, with  $c$  being the speed of light and  $f_c$  the carrier frequency. We consider a multipath channel including  $Q$  delayed, Doppler-shifted, and attenuated copies of the transmitted signal, caused by the  $Q$  scatterers in the environment. As customary in the ISAC literature, we only consider first-order signal reflections and the LoS propagation path, since these are significantly stronger than second-order reflections [30].

Next, we present the Doppler frequency model and the continuous-time channel model underlying the considered scenario. Then, we derive the practical discrete-time channel estimated by the ISAC system.

1) *Doppler frequency model:* The TX movement causes the following instantaneous Doppler shift on the  $q$ -th path

$$f_{D,q}^{\text{tx}}(t) = \frac{1}{\lambda} \frac{\partial}{\partial t} \|\mathbf{x}^{\text{rx}} - \mathbf{x}^{\text{tx}}(t)\| \approx \frac{v^{\text{tx}}(t)}{\lambda} \cos \xi_q(t), \quad (1)$$

where  $\xi_q(t)$  is the angle between the segment connecting the  $q$ -th scatterer to the TX and the TX velocity vector. The approximation in Eq. (1) holds for short processing intervals, during which we consider the movement of the TX to be well approximated by a constant-velocity model [31].

The movement of the target causes an additional Doppler shift on the reflected signal. Specifically, due to the separation of the TX and RX devices in the 2D space, we consider the bistatic Doppler shift,  $f_{D,q}(t)$ , defined as [31]

$$\begin{aligned} f_{D,q}(t) &= \frac{1}{\lambda} \frac{\partial}{\partial t} (\|\mathbf{x}^{\text{rx}} - \mathbf{x}_q(t)\| + \|\mathbf{x}_q(t) - \mathbf{x}^{\text{tx}}(t)\|) \quad (2) \\ &\approx \frac{v_q(t)}{\lambda} \cos \gamma_q(t) \cos \frac{\beta_q(t)}{2}. \quad (3) \end{aligned}$$

Eq. (3) shows that the target-induced bistatic Doppler frequency shift depends on the direction of motion with respect to the bistatic system.

2) *Continuous-time channel model:* Consider the continuous-time channel between the TX and the RX and denote by  $\tau_q(t)$ ,  $\alpha_q(t)$ , and  $A_q(t)$  the propagation delay, the AoD, and the complex coefficient of the  $q$ -th path, respectively.  $A_q(t)$  accounts for the propagation loss, and the scatterer's Radar Cross-Section (RCS) [2]. If the devices are equipped with multiple antennas,  $A_q(t)$  also includes the combined effect of the TX and RX beamforming vectors.

The offsets caused by the asynchrony of TX and RX, i.e., TO, CFO, and PO are denoted by  $\tau_o(t)$ ,  $f_o(t)$ , and  $\psi_o(t)$ ,

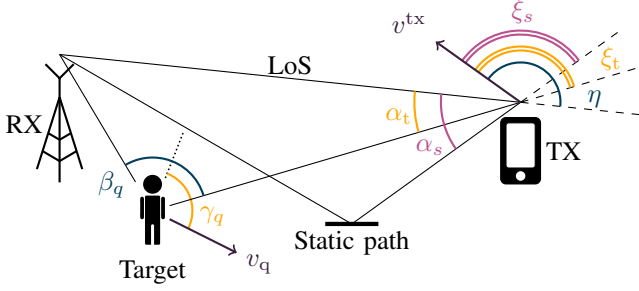


Fig. 2: Reference scenario and multipath geometry. The time dependency is omitted for better visualization.

respectively. Denoting by  $\delta(\tau)$  the Dirac delta function, the CIR at time  $t$  and delay  $\tau$  is

$$h(t, \tau) = e^{j\psi_o(t)} \sum_{q=1}^Q A_q(t) e^{j\vartheta_q(t)} \delta(\tau - \tau_q(t) - \tau_o(t)), \quad (4)$$

where  $\vartheta_q(t) = 2\pi(f_{D,q}(t) + f_o(t) + f_{D,q}^{\text{tx}}(t))t$ . Note that  $f_{D,q}(t)$  is added to the CFO and the Doppler shift introduced by the transmitter.

We stress that even though AsyMov requires estimating the AoD (if the TX is moving) or AoA (if the RX is moving) of the reflections, it does not require having multiple antennas on the ISAC devices. Indeed, our approach is agnostic to the number of available antennas or radio frequency chains at the TX or RX, and can be implemented on cost-effective phased-array systems. In this case, the AoD or AoA can be obtained through correlation-based algorithms such as the ones in [20], [32]. This motivates our choice not to account for multiple antennas explicitly in the channel model.

3) *CIR estimate model*: In Single Carrier (SC) systems, e.g., IEEE 802.11ay, the RX estimates the CIR directly using cross-correlation of the received signal with a known pilot sequence such as complementary Golay sequences which exhibit perfect autocorrelation property with no frequency shift. In Orthogonal Frequency Division Multiplexing (OFDM) systems, e.g., 5G-NR, an estimate of the Channel Frequency Response (CFR) is computed at the receiver by exploiting a known preamble. The CIR can then be obtained via Inverse Discrete Fourier Transform (IDFT) of the estimated CFR.

As a consequence of the finite bandwidth of the ISAC system, two or more scatterers may be closer than the delay resolution, given by  $\Delta_\tau = 1/B$  where  $B$  is the TX signal bandwidth. Hence, we consider a multipath channel including  $M(t) \leq Q$  resolvable components, indexed by  $m = 1, \dots, M(t)$ . The estimated CIR is discretized in the delay domain with granularity  $\Delta_\tau$  and the discrete delay grid is given by  $l\Delta_\tau, l = 0, \dots, L-1$ , where  $L$  is the grid span.

The CIR estimation is repeated across multiple time frames, indexed by  $k$ , at instants  $t_k, k = 0, \dots, K-1$ , where  $K$  is the number of frames and we consider  $t_0 = 0$  s. We denote the inter-frame spacing by  $T_k = t_k - t_{k-1}$ . Note that the inter-frame spacing can be irregular, i.e., channel estimation does not need to happen on a regular sampling grid.

Using a common assumption in ISAC and radar processing, we consider a short processing window of duration  $t_{K-1}$  [30], where the parameters,  $M(t)$ ,  $\tau_m(t)$ ,  $f_{D,m}(t)$ ,

$\alpha_m(t)$ ,  $A_m(t)$ ,  $\eta(t)$ ,  $\xi_m(t)$ ,  $v^{\text{tx}}(t)$ , and consequently the TX motion-induced Doppler shift  $f_{D,m}^{\text{tx}}(t)$  can be considered constant. Conversely, all the nuisance parameters,  $\tau_o(t)$ ,  $f_o(t)$ ,  $\psi_o(t)$ , are time-varying within the window. Note that, although the CFO is sometimes considered slowly time-varying, in ISAC it can significantly drift during the processing window of  $K$  frames. Moreover, in some systems, we need to consider the *residual* CFO after partial compensation by the receiver. The residual CFO is fast time-varying, being the random residual of an imperfect estimation and compensation process [9].

The noise-free estimated CIR at the  $k$ -th frame is

$$h[k, l] = e^{j\psi_o(t_k)} \sum_{m=1}^M A_m e^{j\vartheta_m[k]} \chi(l\Delta_\tau - \tau_m - \tau_o(t_k)), \quad (5)$$

where  $\vartheta_m[k] = 2\pi(f_{D,m} + f_o(t_k) + f_{D,m}^{\text{tx}})t_k$ . In Eq. (5),  $\chi(l\Delta_\tau)$  replaces the Dirac delta to account for non-ideal autocorrelation of the pilot sequence (in SC systems) or the impact of the finite-length CFR estimate (in OFDM systems).

In our scenario, we consider that the  $M$  propagation paths can be partitioned as follows: (i) a LoS path, which represents the direct propagation from the TX to the RX (assumed to be available), (ii) a single moving target path, (iii)  $S$  static scatterers paths for which  $f_{D,m} = 0$ . Point (ii) is not a requirement for AsyMov, but simplifies the derivation. If multiple targets are present, AsyMov should be applied on each corresponding peak in the CIR.

We assume that the orientation of the RX with respect to the TX is known and has been compensated for. This could be done by obtaining the AoD or AoA estimate of the LoS path, for example during beam-alignment protocols for communication. We use this technique in our experimental evaluation in Section VI. If available, an alternative is to use onboard sensors like a gyroscope or an IMU to estimate the device orientation. Using such sensors, the TX could also measure  $v^{\text{tx}}$ , simplifying the derivation of the target's Doppler frequency. However, the accuracy of such measurement is critical to the subsequent estimation process as discussed in [10]. Since low-cost sensors available on commercial cellular devices are often inaccurate, our approach considers  $v^{\text{tx}}$  to be unknown, i.e., it relies on the sole wireless signal. Still, our algorithm can readily incorporate a reliable estimate of  $v^{\text{tx}}$  from an IMU. We demonstrate this in Section VI-E, showing that AsyMov is more accurate when only using the wireless signal, but external IMU measurements enhance its reliability when some multipath components are undetected.

In the following, we focus on estimating the target Doppler frequency under the nuisance due to the CFO, PO, and the TX motion. Hence, we assume that the RX can detect and separate the  $M$  multipath components and extract their phase across time. To this end, the TO can be compensated for by obtaining *relative* delay measurements with respect to the LoS, as done in [10].

### C. Phase measurements

In this section, we provide a model of the phase for each multipath component in Eq. (5). To simplify the notation,

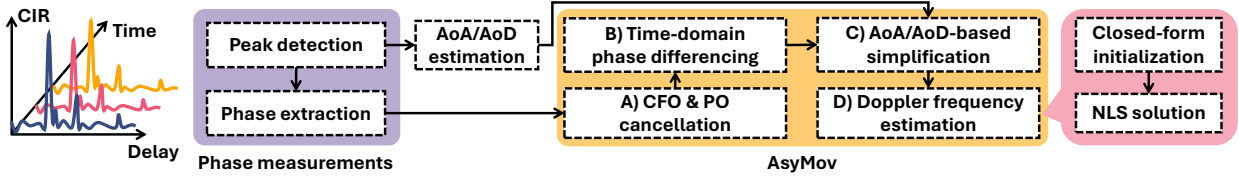


Fig. 3: Block diagram of the proposed phase measurements steps and algorithm.

we omit noise in the channel estimate, but we consider it in Section IV-D when presenting our method.

We group the CFO and PO terms, which are the same on all propagation paths, into  $\Psi_o(t_k) = \psi_o(t_k) + 2\pi f_o(t_k)t_k$ . Moreover, we use subscripts  $\cdot_{\text{LoS}}$  and  $\cdot_t$  to refer to quantities related to the LoS and to the target-induced paths, respectively, as shown in Fig. 2. For the paths caused by static scatterers, we use index  $s = 1, \dots, S$ , where  $S$  is the number of resolvable static scatterers detected in the processing window, with  $S = M - 2$ . The noise-free phase of the LoS is

$$\phi_{\text{LoS}}[k] = \Psi_o(t_k) + \angle A_{\text{LoS}} + 2\pi t_k \left( \frac{v^{\text{tx}}}{\lambda} \cos \eta \right), \quad (6)$$

where  $\angle \cdot$  is the phase operator and we substitute  $\xi_{\text{LoS}} = \eta$ . The noise-free phase of the target-induced path is affected by both the Doppler shift caused by the target ( $f_{\text{D},t}$ ) and by the TX motion ( $v^{\text{tx}}$ ) as

$$\phi_t[k] = \Psi_o(t_k) + \angle A_t + 2\pi t_k \left( f_{\text{D},t} + \frac{v^{\text{tx}}}{\lambda} \cos \xi_t \right), \quad (7)$$

where  $\xi_t$  is the angle between the segment connecting the target to the TX and the TX velocity vector. The phase of the  $s$ -th static multipath component is

$$\phi_s[k] = \Psi_o(t_k) + \angle A_s + 2\pi t_k \left( \frac{v^{\text{tx}}}{\lambda} \cos \xi_s \right). \quad (8)$$

From the CIR, the RX measures  $\text{mod}_{2\pi}(\phi_i[k])$  where  $i \in \{t, \text{LoS}, s\}$ ,  $k = 0, \dots, K - 1$ , and  $\text{mod}_{2\pi}(\cdot)$  is the modulo  $2\pi$  division, whose result is in  $[0, 2\pi)$ .

#### IV. METHODOLOGY

In this section, we introduce AsyMov, which estimates the bistatic Doppler frequency of the target from the phase measurements in Eqs. (6-8). The phase measurements are extracted from the CIR estimate as described in the previous section and shown in the left part of Fig. 3. The processing steps carried out by AsyMov are shown in the yellow block in Fig. 3 and can be summarized as follows.

**A. CFO and PO cancellation.** The phase offsets component,  $\Psi_o$ , is common to all propagation paths. Hence, we can subtract the phase of the LoS path from the other phase measurements, by *canceling out*  $\Psi_o$ . This step does not require a direct estimation of the phase offsets, enabling coherent processing of the multipath components with minimal complexity. This is further detailed in Section IV-A.

**B. Time-domain phase differencing.** By computing time-domain phase differences for each path, we cancel out the path-specific phase terms due to the complex path amplitudes,  $\angle A_i$ , with  $i \in \{t, \text{LoS}, s\}$ , as detailed in Section IV-B. The

resulting phase differences only depend on the Doppler shifts due to the TX and the target.

**C. AoD-based simplification.** We leverage AoD estimation at the TX and the multipath geometry to make a key simplification in the phase measurements model, as described in Section IV-C. This reduces the number of unknowns, thus enabling the estimation of the target Doppler frequency if at least 2 static multipath components are detected.

**D. Doppler frequency estimation.** Using the simplified phase measurements model, we formulate the estimation of the target's Doppler frequency as a vector Nonlinear Least-Squares (NLS) problem across the multipath components (see Section IV-D). To initialize the NLS, we derive and use the closed-form solution of the model using  $S = 2$  static paths.

##### A. CFO and PO cancellation

To cancel out the phase offsets term,  $\Psi_o$ , we subtract  $\phi_{\text{LoS}}[k]$  from  $\phi_t[k]$  and  $\phi_s[k]$ , obtaining

$$\tilde{\phi}_t[k] = \Omega_t + 2\pi t_k \left( f_{\text{D},t} + \frac{v^{\text{tx}}}{\lambda} (\cos \xi_t - \cos \eta) \right), \quad (9)$$

$$\tilde{\phi}_s[k] = \Omega_s + 2\pi t_k \left( \frac{v^{\text{tx}}}{\lambda} (\cos \xi_s - \cos \eta) \right), \quad (10)$$

where  $\Omega_s = \angle A_s - \angle A_{\text{LoS}}$ ,  $\Omega_t = \angle A_t - \angle A_{\text{LoS}}$ . Computing phase differences *cancel out* CFO and PO without estimating them, since they are common to all propagation paths. Despite the absence of CFO and PO in Eq. (9), the estimation of the target's Doppler frequency remains non-trivial due to the presence of the undesired frequency term  $v^{\text{tx}} (\cos \xi_t - \cos \eta) / \lambda$  caused by the receiver movement. Indeed, a direct application of standard Fourier-based processing to estimate the Doppler frequency would fail to separate  $f_{\text{D},t}$  from the Doppler due to the TX movement.

##### B. Time-domain phase differencing

After CFO and PO cancellation, the RX computes first-order time-domain phase differences as

$$\Delta_i[k] = \text{mod}_{2\pi}(\tilde{\phi}_i[k]) - \text{mod}_{2\pi}(\tilde{\phi}_i[k-1]) \quad (11)$$

with  $i \in \{t, s\}$  and  $k = 1, \dots, K - 1$ . The phase differences are expressed as

$$\Delta_t[k] = 2\pi T_k \left( f_{\text{D},t} + \frac{v^{\text{tx}}}{\lambda} (\cos \xi_t - \cos \eta) \right), \quad (12)$$

$$\Delta_s[k] = 2\pi T_k \left( \frac{v^{\text{tx}}}{\lambda} (\cos \xi_s - \cos \eta) \right), \quad (13)$$

where we recall that  $T_k = t_k - t_{k-1}$ .

In Eq. (12) and Eq. (13), we assume that the inter-frame spacing for channel estimation,  $T_k$ , is sufficiently small so that

the phase change between two subsequent frames is smaller than  $\pi$ . This allows writing phase differences without the ambiguity due to the  $\text{mod}_{2\pi}$  operator. From Eq. (12), it can be seen that the noise-free phase differences  $\Delta_t$  and  $\Delta_s$  are upper bounded by  $2\pi T_k(3f_{\max})$ , with  $i \in \{t, s\}$  and  $f_{\max}$  being the maximum Doppler shift caused by the TX (or the target).  $f_{\max}$  is a system design parameter that can be set depending on the specific scenario and application. To fulfill the assumption, it is sufficient to impose  $|\Delta_i| < \pi$  which yields  $T_k < 1/(6f_{\max})$ . The choice of  $T_k$  is further discussed in Section V.

### C. AoD-based simplification

By inspecting Fig. 2, a key simplification can be made in Eq. (12) and Eq. (13) noticing that  $\cos \xi_i = \cos(\eta - \alpha_i) = \cos(\alpha_i - \eta)$ , with  $i \in \{t, s\}$ . This substitution removes the dependency on the unknown and path-dependent angle  $\xi_i$ . The new expressions of the phase differences are

$$\Delta_t[k] = 2\pi T_k \left( f_{D,t} + \frac{v^{\text{tx}}}{\lambda} (\cos(\eta - \alpha_t) - \cos \eta) \right), \quad (14)$$

$$\Delta_s[k] = 2\pi T_k \left( \frac{v^{\text{tx}}}{\lambda} (\cos(\eta - \alpha_s) - \cos \eta) \right), \quad (15)$$

where the new dependency on  $\alpha_i - \eta$ , for  $i \in \{t, s\}$ , is easier to handle since the RX estimates  $\alpha_i$  and the unknown term  $\eta$  is independent of the propagation paths. Note that, since the RX estimates  $\alpha_s$  and  $\alpha_t$ , this operation reduces the unknowns from  $S + 4$ , i.e.,  $f_{D,t}, v^{\text{tx}}, \eta, \xi_t, \xi_1, \dots, \xi_S$ , to 3, i.e.,  $f_{D,t}, v^{\text{tx}}, \eta$ . This makes Eq. (12) and Eq. (13), for  $s = 1, \dots, S$ , a set of  $S + 1$  equations with 3 unknowns, which can be solved if the number of static multipath components satisfies  $S \geq 2$ . In the next section, we provide our solution based on NLS.

### D. Doppler frequency estimation

We reformulate Eq. (14) and Eq. (15) as

$$\tilde{\Delta}_t[k] = f_{D,t} + \frac{v^{\text{tx}}}{\lambda} (\cos(\eta - \alpha_t) - \cos \eta), \quad (16)$$

$$\tilde{\Delta}_s[k] = \frac{v^{\text{tx}}}{\lambda} (\cos(\eta - \alpha_s) - \cos \eta), \quad (17)$$

where  $\tilde{\Delta}_i[k] = \Delta_i[k]/(2\pi T_k)$ , for  $i \in \{t, s\}$ . Then, we define the following vector quantities: the phase differences vector at the  $k$ -th frame,  $\tilde{\Delta}[k] = [\tilde{\Delta}_t[k], \tilde{\Delta}_1[k], \dots, \tilde{\Delta}_S[k]]^\top$ , the unknown parameter vector  $\theta = [f_{D,t}, \eta, v^{\text{tx}}]^\top$ , and the non-linear vector function  $\mathbf{g}(\theta)$ , which expresses the non-linear relations in Eq. (16) and Eq. (17). The following model holds

$$\tilde{\Delta}[k] = \mathbf{g}(\theta) + \mathbf{w}[k], \quad (18)$$

where  $\mathbf{w}[k]$  is a complex-valued Gaussian noise vector with diagonal covariance matrix  $\mathbf{C}_k$  whose elements are the variances  $\sigma_{t,k}^2, \sigma_{1,k}^2, \dots, \sigma_{S,k}^2$ . A more precise characterization of the noise vector will be given in Section V. To reduce the impact of noise, we average the measured phase differences over time obtaining  $\bar{\Delta} = \sum_{k=1}^{K-1} \tilde{\Delta}[k]/(K-1)$ .

1) *Nonlinear least-squares solution:* An NLS problem is solved to retrieve an estimate of the unknown parameters

$$\hat{\theta} = \arg \min_{\theta} \|\bar{\Delta} - \mathbf{g}(\theta)\|_2^2, \quad (19)$$

from which we get the Doppler frequency estimate as the first component of the solution, which we denote by  $\hat{f}_{D,t}$ . This problem can be solved using, e.g., the Levenberg-Marquardt algorithm with a suitable initialization [33]. The computational complexity of the algorithm is  $O(d_{\theta}^2(S+1)N_{\text{it}})$ , where  $d_{\theta} = 3$  is the dimension of  $\theta$  and  $N_{\text{it}}$  represents the number of iterations needed to converge.

2) *Closed form solution:* Consider Eq. (17) with 2 phase measurements from static paths, i.e.,  $s \in \{1, 2\}$ . We denote by  $\bar{\Delta}_t, \bar{\Delta}_1$ , and  $\bar{\Delta}_2$  the time-averaged phase differences for the sensing path, and static paths 1 and 2. Using also Eq. (16), a system with 3 equations in 3 unknowns is attained, which can be solved for  $\theta$ . We provide the solution in Appendix A, giving the full expressions of  $\hat{\eta}$  and  $\hat{v}^{\text{tx}}$ . The expression of  $\hat{f}_{D,t}$  is

$$\hat{f}_{D,t} = \bar{\Delta}_t - \bar{\Delta}_1 \frac{\cos(\alpha_t - \hat{\eta}) - \cos \hat{\eta}}{\cos(\alpha_1 - \hat{\eta}) - \cos \hat{\eta}}. \quad (20)$$

The solution requires the following conditions to be met: (i)  $\alpha_i \neq 0, i \in \{1, 2, t\}$ , (ii)  $\alpha_i \neq \alpha_{\ell}, i \neq \ell \in \{1, 2, t\}$ , and (iii)  $\alpha_i \neq 2\hat{\eta}, i \in \{1, 2\}$ . Note that violating conditions (i) and (ii) correspond to degenerate scenarios in which the LoS path is not available, or two static multipath components have the same AoD. Condition (iii) instead is violated if the AoD of one of the multipath components is equal to  $2\hat{\eta}$ .

## V. ANALYSIS AND NUMERICAL SIMULATIONS

In this section, we derive the CRLB on the estimation of the parameter vector  $\theta$ , based on the measurement model in Eq. (16) and Eq. (17). Then, we describe our simulations and the obtained numerical results.

### A. Noise characterization

Before deriving the CRLB, we characterize vector  $\mathbf{w}[k]$ , which represents the noise on the phase measurements after the phase offsets removal and time-domain differencing (Eq. (16) and Eq. (17)). We assume the noise on the received signal is distributed as a complex Gaussian with variance  $\sigma_w^2$ . The channel estimation process reduces the noise variance by aggregating multiple pilot symbols coherently. The noise variance on the CIR is  $\sigma_h^2 = \sigma_w^2/G$  where  $G$  is proportional to the number of pilot symbols.

The noise on the phase measurements in Eqs. (6-8) depends the noise on the CIR through a non-linear relation. Denote path  $i$  in the estimated CIR in Eq. (5) at frame  $k$  by  $h_i[k, l_i] \approx A_i e^{j(\theta_i[k] + \psi_o(t_k))}$ , with  $i \in \{\text{LoS}, t, s\}$ .  $l_i$  is the index of the peak corresponding to the  $i$ -th path and  $l_i \Delta \tau \approx \tau_i$ . The real and imaginary components of  $h_i[k, l_i]$  are denoted by  $\Re\{h_i\}$  and  $\Im\{h_i\}$ , respectively. The phase of the  $i$ -th CIR path is given by  $\angle h_i[k, l_i] = \arctan(\Im\{h_i\}/\Re\{h_i\})$ . For small values of  $\sigma_h^2$ , we can linearize the arctan function and approximate the resulting noise random variable as Gaussian.

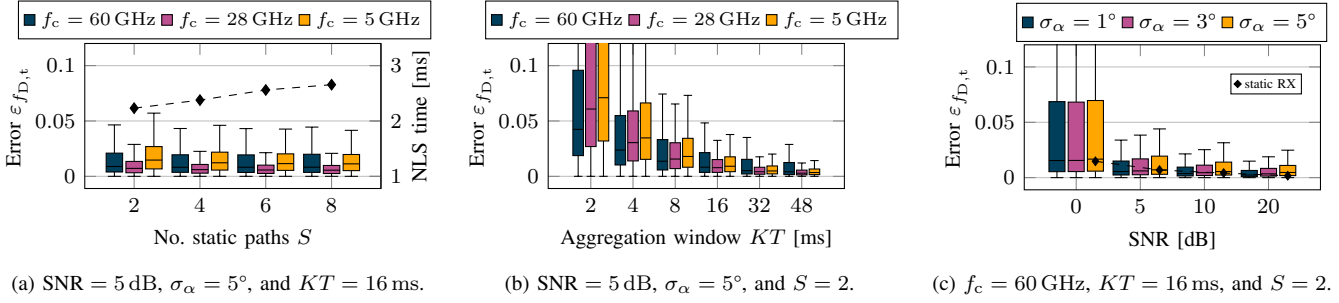


Fig. 4: Target Doppler frequency estimation error varying the number of available static scatterers, the duration of the processing window, the SNR, and the AoAs measurements error, with  $f_c = 60$  GHz,  $f_c = 28$  GHz, and  $f_c = 5$  GHz.

In this case, the noise variance on path  $i \in \{\text{LoS}, t, s\}$  is given by  $\sigma_i^2 = \sigma_h^2 / (2|A_i|^2)$  (the derivation is given in Appendix C).

The noise on the phase measurements is further affected by the CFO and PO removal and time-domain differencing operations. The phase offsets removal subtracts the phase of the LoS path from the phases of the other paths, hence increasing the variance of the noise on phase  $i \in \{t, s\}$  to

$$\sigma_{\phi,i}^2 = \sigma_{\phi,i}^2 + \sigma_{\text{LoS}}^2 = \frac{\sigma_h^2}{2} \left( \frac{1}{|A_i|^2} + \frac{1}{|A_{\text{LoS}}|^2} \right) = \frac{\sigma_h^2}{2} \kappa_i, \quad (21)$$

where we defined  $\kappa_i = |A_i|^{-2} + |A_{\text{LoS}}|^{-2}$ . The time-domain differencing operation in Section IV-B doubles the noise variance, which we assume to be constant across time, giving  $\sigma_{\Delta,i}^2 = 2\sigma_{\phi,i}^2$ . Finally, dividing the phase measurements by the inter-frame spacing, as done in Section IV-D, makes the noise variance depend on the specific frame  $k$ . Hence, the variances  $\sigma_{i,k}^2, i \in \{t, s\}$  that constitute the covariance matrix  $\mathbf{C}_k$  of vector  $\mathbf{w}[k]$  are

$$\sigma_{i,k}^2 = \frac{\sigma_{\Delta,i}^2}{4\pi^2 T_k^2} = \frac{\sigma_w^2 \kappa_i}{4\pi^2 G T_k^2}. \quad (22)$$

### B. Performance limits analysis

To assess bounds on the performance of the proposed Doppler frequency estimation method, we use the CRLB [34], which represents a lower bound on the error variance of the estimate of  $\boldsymbol{\theta}$ . In the CRLB derivation, we assume no prior knowledge of the parameters  $\boldsymbol{\theta}$  is available and we consider each path's AoD to be known exactly since the latter is an input to our algorithm and must be obtained by other means. Moreover, to simplify the derivation and make the expressions more compact, we restrict to the case  $S = 2$ , i.e., two static paths are available, and we consider only a single time frame  $k$ .

The likelihood of the vector measurement model in Eq. (18) is a multivariate Gaussian

$$p(\tilde{\Delta}[k]; \boldsymbol{\theta}) \sim \mathcal{N}(\tilde{\Delta}[k] - \mathbf{g}(\boldsymbol{\theta}), \mathbf{C}_k) \quad (23)$$

where  $\mathbf{C}_k$  is a diagonal matrix with elements  $\sigma_{t,k}^2, \sigma_{1,k}^2, \sigma_{2,k}^2$ .

Element  $\nu, \nu$  of the Fisher Information Matrix (FIM),  $\mathbf{J}$ , is [34]  $[\mathbf{J}]_{\nu,\nu} = -E[\partial^2 \log \mathcal{L}(\boldsymbol{\theta}) / \partial \theta_\nu \partial \theta_\nu]$ . We give the full expression of the FIM elements in Appendix C, in Eqs. (35-37). By inverting matrix  $\mathbf{J}$ , and taking the first element on the diagonal,  $[\mathbf{J}^{-1}]_{1,1}$ , we obtain the CRLB on the Doppler frequency of the target, given by

$$[\mathbf{J}^{-1}]_{1,1} = \frac{\sigma_w^2 \zeta_{t,1,2}}{128\pi^2 G T_k^2 \sin\left(\frac{\alpha_1}{2}\right) \sin\left(\frac{\alpha_1 - \alpha_2}{2}\right) \sin\left(\frac{\alpha_2}{2}\right)}, \quad (24)$$

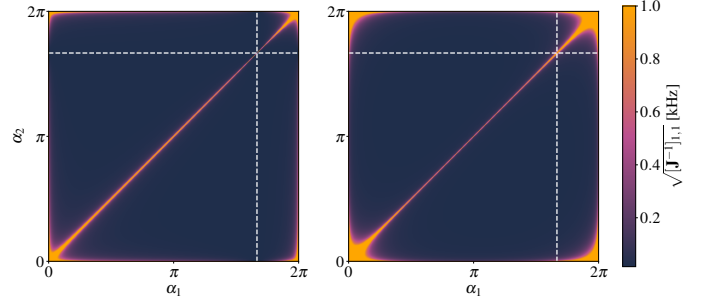


Fig. 5: Square-root CRLB example: exact value (left), and upper bound from Eq. (25) (right). White dashed lines correspond to the value of  $\alpha_t$  used to generate the plot. For visualization, values higher than 1 kHz are clipped.

where  $\zeta_{t,1,2}$  is given in Appendix C, in Eq. (38), and exhibits a complex dependency on  $\kappa_t, \kappa_1, \kappa_2$  and the AoDs,  $\alpha_t, \alpha_1, \alpha_2$ . To simplify the analysis and provide a useful expression of practical interest, we derive an upper bound to  $\zeta_{t,1,2}$ , given by  $\zeta_{t,1,2} < 18 \sum_{i \in \{t,1,2\}} \kappa_i$ . The derivation consists in substituting the extremal values,  $\{+1, -1\}$ , assumed by the cosine terms in Eq. (38). Using this simplification and plugging into Eq. (32) gives an upper bound for the CRLB

$$[\mathbf{J}^{-1}]_{1,1} < \frac{9\sigma_w^2 \sum_{i \in \{t,1,2\}} \kappa_i}{64\pi^2 G T_k^2 \sin\left(\frac{\alpha_1}{2}\right) \sin\left(\frac{\alpha_1 - \alpha_2}{2}\right) \sin\left(\frac{\alpha_2}{2}\right)}. \quad (25)$$

In Fig. 5, we show the square root of the exact CRLB, Eq. (24), and the upper bound, Eq. (25), as a function of the AoDs of the static paths,  $\alpha_1, \alpha_2$ . The other parameters are instead set as  $\alpha_t = 5\pi/3$  rad,  $|A_t| = 0.05$ ,  $|A_1| = |A_2| = 0.2$ ,  $|A_{\text{LoS}}| = 0.1$ ,  $T_k = 0.25$  ms. We observe that  $[\mathbf{J}^{-1}]_{1,1} \rightarrow +\infty$  when  $\alpha_1, \alpha_2 \rightarrow 2n\pi, n \in \mathbb{N}_0$  and  $\alpha_1 \rightarrow \alpha_2$ . This makes two of the equations in Eq. (18) equal, making the system underdetermined. Finally, note that Eq. (24) does not contain  $v^{\text{tx}}$  and  $\eta$ , making it independent of the TX velocity vector. This means that the minimum estimation error on the Doppler frequency is not influenced by the magnitude or direction of the TX velocity.

### C. Simulation setup

To validate AsyMov we perform simulations for 5 GHz, 28 GHz, and 60 GHz carrier frequencies  $f_c$ , as representative of, e.g., IEEE 802.11ax, Frequency Range 2 (FR2) 5G-NR, and IEEE 802.11ay systems, respectively. The coordinates of the target and static objects are randomly generated in a  $d \times d$  empty mobility area and the real CIR is obtained using

TABLE 1: Simulation parameters used in the numerical results.  $\mathcal{U}(a, b)$  denotes the uniform distribution in the interval  $[a, b]$ . Values in curly brackets refer to the parameters used for 60, 28, and 5 GHz carrier frequencies, respectively.

Target Doppler frequency [Hz]	$f_{D,t}$	$\pm\mathcal{U}(f_{\min}, f_{\max})$
Receiver velocity [m/s]	$v^{\text{rx}}$	$\mathcal{U}(v_{\min}, v_{\max})$
Min. TX/target Doppler freq. [Hz]	$f_{\min}$	100
Min. TX/target velocity [m/s]	$v_{\min}$	0.5
Max. TX/target Doppler freq. [kHz]	$f_{\max}$	{1, 0.93, 0.3}
Max. TX/target velocity [m/s]	$v_{\max}$	{5, 10, 20}
Mobility area side [m]	$d$	{20, 50, 100}
Carrier wavelength [cm]	$\lambda$	{0.5, 1.07, 6}
Channel estimation period [ms]	$T$	{0.166, 0.178, 0.5}
Bandwidth [GHz]	$B$	{1.76, 0.4, 0.16}
Subcarrier spacing [kHz]	–	{–, 120, 78.125}
CFO time difference stand. dev. [MHz]	$\sigma_o$	{0.22, 0.12, 0.02}

Eq. (4). Hence, we simulate the transmission of the waveform used to perform channel estimation. For  $f_c = 60$  GHz, an IEEE 802.11ay TRN field made of complementary Golay sequences is transmitted, while for  $f_c = 5$  GHz and  $f_c = 28$  GHz, we employ a random sequence of OFDM symbols modulated with BPSK. At the receiver, we add CFO, PO, and channel noise according to different SNR values. The received signal is sampled with period  $1/B$  and the CIR is estimated. After the peak detection operation, the phases of the CIR peaks and the noisy AoD estimates, for each available path, are inputted into our model. All the parameters are summarized in Tab. 1. The maximum TX speed,  $v_{\max}$ , differs for each carrier frequency to reflect the typical speed of the corresponding use case, i.e., IEEE 802.11ax, 5G-NR and IEEE 802.11ay. Finally, to consistently compare various simulation configurations, we set the inter-frame spacing  $T_k$  to a fixed value  $T_k = T = 1/(6f_{\max})$ , which is the maximum time gap allowed in the measurements to avoid phase ambiguity, as discussed in Section IV-B. We remark that the selected  $T$  is compatible with existing hardware and typical packet transmission times in wireless networks. The residual CFO is modeled as  $f_o(kT) \sim \mathcal{N}(0, \sigma_o^2)$ , where  $\sigma_o^2$  is chosen such that the frequency shift in 1 ms is between  $\pm 0.1$  parts-per-million (ppm) of the carrier frequency  $f_c$  [35]. The PO is modeled as  $\psi_o(kT) \sim \mathcal{U}(0, 2\pi)$ . Note that our method cancels out the CFO and PO *exactly*, hence it is not significantly affected by their magnitude. The error on the AoD estimates is modeled as an additive Gaussian r. v. with distribution  $\mathcal{N}(0, \sigma_\alpha^2)$ .

#### D. Doppler frequency estimation performance

Next, we evaluate the performance of our Doppler frequency estimation algorithm in terms of normalized absolute estimation error, defined as  $\varepsilon_{f_{D,t}} = |f_{D,t} - \hat{f}_{D,t}|/|f_{D,t}|$ .

1) *Number of static scatterers*: The number of available static scatterers  $S$  is of prime importance for the proposed algorithm, as detailed in Section IV-D1. In fact, a minimum of  $S = 2$  static paths are needed for the algorithm to admit a solution, whereas  $S > 2$  increases its robustness. This is confirmed by the results in Fig. 4a, where we show that the median estimation error and its spread are reduced if more static scatterers are available. Remarkably, beyond  $S = 4$

the performance improvement is modest. For every considered carrier frequency, the median error lies below 2% of the actual Doppler frequency, even with  $S = 2$ . We recall that each scatterer adds one equation to the NLS problem of Eq. (19) without increasing the number of unknowns. This leads to a more robust, whilst more complex to compute, solution. In Fig. 4a, black diamonds represent the average time (across all  $f_c$ ) needed to solve the NLS problem on an Intel Core i7-9700 CPU, by varying  $S$ .

2) *Processing window duration*: In Fig. 4b, we evaluate the impact of averaging phase measurements over a longer aggregation window. We underline that, since  $T$  differs for each carrier frequency, for a fixed observation interval  $KT$  every considered  $f_c$  entails a different number of phases and AoD estimates that are collected. Increasing the number of considered frames  $K$ , while keeping  $T$  constant, clearly improves robustness to noise. However, the window duration can not be made arbitrarily large but has to be tuned depending on the dynamicity of the environment to ensure that the channel parameters remain constant through the whole observation interval  $KT$ . With  $KT = 32$  ms, our method provides a median error below 1% of the true Doppler frequency for every considered  $f_c$ . This result could be further improved by combining estimates across subsequent time windows.

3) *Measurements error*: In Fig. 4c, we show the Doppler frequency estimation error as a function of the SNR, and of the noise affecting AoD measurements ( $\sigma_\alpha$ ). Lower SNR values greatly increase the estimation error spread, despite its median remaining below 0.02. Fig. 4c also shows that  $f_{D,t}$  is slightly affected by the AoD error, which means that the SNR level has a much stronger impact. As a reference for comparison, we also plot the median  $\varepsilon_{f_{D,t}}$  for a *static* TX.

Although our work focuses on Doppler frequency estimation, AsyMov also obtains estimates for  $\eta$  and  $v^{\text{tx}}$ . In Fig. 7, we show the normalized estimation errors for  $\eta$  and  $v^{\text{tx}}$ , which are respectively evaluated as  $\varepsilon_\eta = |\eta - \hat{\eta}|/|\eta|$  and  $\varepsilon_{v^{\text{tx}}} = |v^{\text{tx}} - \hat{v}^{\text{tx}}|/|v^{\text{tx}}|$ , where  $\hat{\eta}$  and  $\hat{v}^{\text{tx}}$  respectively represent the estimated TX movement direction angle and the estimated TX speed.

4) *CIR measurement interval analysis*: As discussed in Section IV-B,  $T$  has to be sufficiently small to prevent ambiguity in the phase measurements. However, decreasing  $T$  makes the phase differences more sensitive to noise due to the structure of Eq. (22). So, a suitable tradeoff has to be identified. The impact of an increasing  $T$  on the estimation error due to the occurrence of phase ambiguities is evaluated in Fig. 8a. Here,  $T$  starts from the maximum value for which phase ambiguities are prevented. As expected, increasing  $T$  beyond this value causes a growth in the estimation error  $\varepsilon_{f_{D,t}}$ . Fig. 8a is obtained for  $f_c = 60$  GHz by way of example, but similar results hold for other carrier frequencies.

## VI. EXPERIMENTAL RESULTS

In this section, we present experimental results obtained by AsyMov on an IEEE 802.11ay-based ISAC testbed.



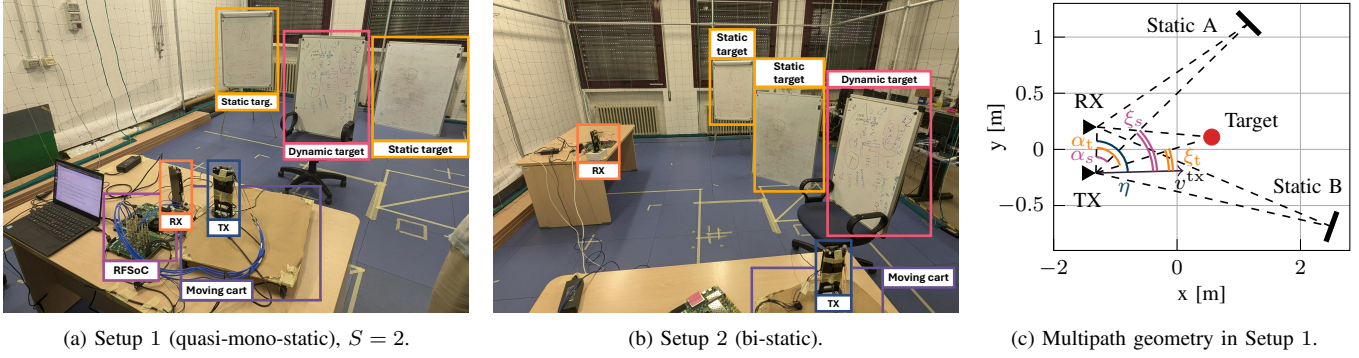


Fig. 6: Visualization of the experimental setup.

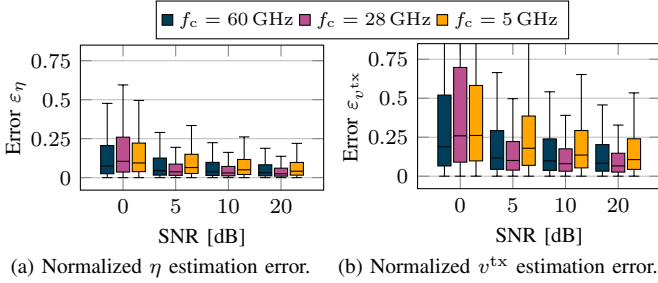


Fig. 7: Varying SNR values, with  $\sigma_\alpha = 5^\circ$ ,  $KT = 16$  ms, and  $S = 2$ .

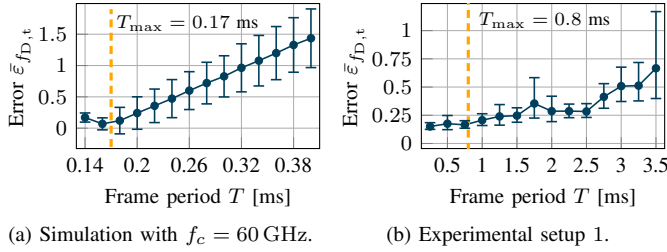


Fig. 8: Average normalized Doppler frequency error.

### A. ISAC testbed

Our testbed consists of two ISAC nodes acting as TX and RX. Each node comprises a Xilinx RFSoc for baseband signal processing and a mmWave Siivers 16-elements phased array antennas operating at  $f_c = 60$  GHz. The implementation is based on that presented in [10], which is an adaptation of MIMORPH [36], an open-source project for mmWave experimentation. We refer to [10], [36] for additional details on the testbed setup.

The TX sends IEEE 802.ay standard-compliant packets with 1.76 GHz bandwidth, including an IEEE 802.11ay header and a TRN field. This field contains 12 TRN units, each composed of 6 complementary Golay sequences [37]. We use each TRN unit to estimate the channel for a different TX beam pattern, scanning the whole angular space in front of the TX. This allows us to estimate the AoD of each multipath component in the subsequent signal-processing phase. The antenna beamwidth determines the resolution of the AoD estimation, which approximately equals  $8^\circ$ . The RX performs downconversion, sampling, packet detection, and symbol-level synchronization. After that, I/Q samples are stored and processed offline with Matlab scripts to perform channel estimation. The channel estimates are then fed to

the proposed algorithm, which is implemented in Python. Sampling at the RX side is carried out using a frequency of 3.52 GHz, fulfilling the requirements of mmWave IEEE 802.11ad/ay. Packet detection is performed by computing the autocorrelation of the received signal and checking whether this exceeds a pre-defined threshold [36], [38]. To perform CIR estimation we compute the cross-correlation of the received signal with the known TRN units at the RX. Then, we apply peak detection to isolate significant multipath components and estimate AoD for each peak using the algorithm in [20]. We compensate for the TX orientation by estimating the AoD of the LoS path and removing it from the AoD of other paths.

To demonstrate the capability of the proposed algorithm to incorporate velocity measurements from onboard sensors on the ISAC devices, we equip the TX with an IMU mounted on the back of the phased antenna array. To this end, we use a Phidget MOT110 IMU device, synchronized with the transmission of the wireless signal. This provides measurements of the TX velocity vector according to a reference frame centered on the TX device. Results obtained by integrating IMU measurements with our algorithm are presented in Section VI-E.

### B. Experimental setup

The experiments are performed in a  $5 \times 4$  m laboratory equipped with an infrared camera-based motion tracking system, as shown in Fig. 6. The camera system allows obtaining the accurate positions of each object in the environment to be used as a ground-truth reference. For this, we place infrared markers on the TX, RX, static reflectors, and targets. Metal whiteboards are used to produce both static and dynamic reflections. One of the whiteboards is mounted on a wheeled chair to allow moving it during the experiments, serving as the dynamic target (which is the objective of the Doppler frequency estimation process). Similarly, we place the TX on a wheeled cart, moving it during the measurements. In all the considered experiments, the motion of the target and the TX was generated by moving the chair and cart back and forth at a random speed in an uncoordinated fashion. We do not use rails or other methods to produce straight and regular trajectories, thus simulating a more realistic case in which ISAC devices may be handheld and targets follow irregular trajectories.

We consider 2 different evaluation setups, as described next.

- *Setup 1 (SU1)*. As shown in Fig. 6a, the first setup includes quasi-monostatic TX and RX, placed at a distance of 40 cm

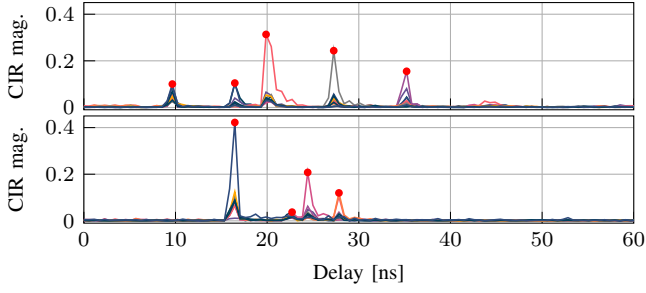


Fig. 9: Peak detection in Setup 1 with  $S = 3$  (top) and in Setup 2 with  $S = 2$  (bottom). Different curves correspond to TX beam patterns, while red dots mark the peaks.

from one another and oriented towards the targets. We consider the cases of  $S = 2$  and  $S = 3$  static targets available, by adding a third whiteboard when  $S = 3$ . In Fig. 9, we show an example of the estimated CIR with  $S = 3$  for Setup 1.

- *Setup 2 (SU2)*. A more challenging evaluation is conducted in a bi-static setting, with widely separated TX and RX, as shown in Fig. 6b. This experiment reproduces more realistic conditions in which the LoS path is weaker and the orientation of the ISAC devices is unknown. In the bottom plot in Fig. 9, we show an example of the estimated CIR with  $S = 2$  for Setup 2. The reflection from the moving target is considerably weaker than in Setup 1, making this second setup significantly more challenging. To mitigate the stronger noise of this configuration, we applied a Savitzky-Golay filter with a window of 250 ms to the target Doppler estimate.

In our experiments, the maximum speed achievable by the TX and the target is much lower than that considered in our simulations (see Section V-C). Hence, we rescale parameters  $v_{\max}$  and  $f_{\max}$  accordingly, setting  $v_{\max} = 1$  m/s and  $f_{\max} = 200$  Hz. Unless specified, we consider the inter-frame duration  $T_k$  to be constant and denote it by  $T = 0.254$  ms. In Section VI-C1, we show that this simplification is not restrictive, since AsyMov is robust to a random choice of  $T_k$ . Furthermore, in the experiments, we re-analyze the choice of the inter-frame duration  $T$  to avoid phase ambiguities. As shown in Fig. 8b, due to the lower velocities involved, AsyMov achieves good performance on the experiments in Setup 1 for up to  $T = 0.8$  ms. The performance degradation is minimal up to  $T = 2.5$  ms due to the lower variations in Doppler frequencies observed in the experiments (as compared to the simulations), which leads to a lower probability of experiencing phase ambiguities.

### C. Doppler frequency and TX speed estimation error

The performance of AsyMov is evaluated using the absolute estimation errors on the Doppler frequency of the target, the TX speed, and  $\eta$ , respectively defined as  $\hat{\varepsilon}_{f_{D,t}} = |f_{D,t} - \hat{f}_{D,t}|$ ,  $\hat{\varepsilon}_{v^{\text{tx}}} = |v^{\text{tx}} - \hat{v}^{\text{tx}}|$ ,  $\hat{\varepsilon}_{\eta} = |\eta - \hat{\eta}|$ . The ground truth  $f_{D,t}$  is obtained by plugging in Eq. (3) the ground truth locations of the TX, the RX, and the target, obtained from the motion tracking system.

1) *Results for Setup 1*: In the top plot of Fig. 10, we show the ground truth and the estimated target Doppler frequency for a specific experiment in Setup 1. We also show the

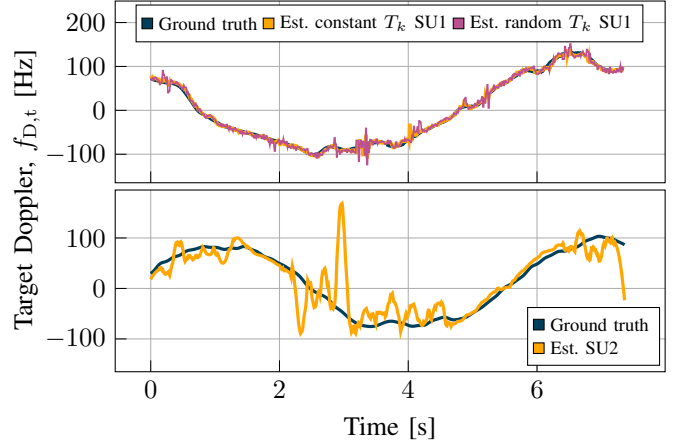


Fig. 10: Estimated target Doppler frequency,  $\hat{f}_{D,t}$ , with  $S = 2$  and  $KT = 16$  ms, for Setup 1 (top) and Setup 2 (bottom).

TABLE 2: Average target Doppler frequency estimation error  $\pm$  one standard deviation, in different setups with  $KT = 16$  ms.

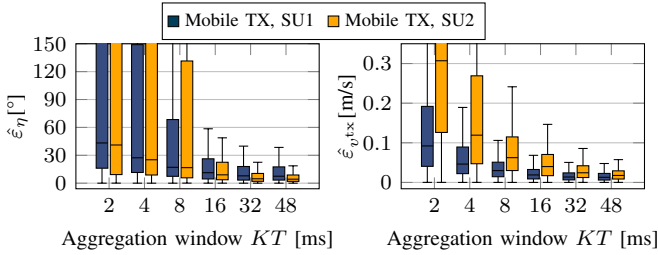
Error [Hz]	SU1, $S = 2$	SU1, $S = 3$	SU2, $S = 2$
Mobile	$2.84 \pm 2.63$	$2.84 \pm 2.63$	$18.28 \pm 22.02$
Static	$2.18 \pm 1.87$	$2.18 \pm 1.87$	$18.17 \pm 19.23$

results obtained with a random inter-frame spacing  $T_k$ . This case is implemented by randomly discarding CIR estimates in the experiment – each element is independently discarded with probability 0.5. AsyMov can accurately estimate the target Doppler frequency, with a marginal degradation with a random  $T_k$ . Specifically, AsyMov obtains Doppler frequency estimation errors of  $3.03 \pm 3.61$  and  $5.07 \pm 6.66$  with constant and random  $T_k$ , respectively (mean  $\pm$  one standard deviation). The slight degradation of the latter (random) case is due to the fewer samples available in the observation window, as a consequence of the removal of CIR samples.

In the following, we provide results on the Doppler frequency estimation error,  $\hat{\varepsilon}_{f_{D,t}}$ , in Tab. 2, on the TX movement direction,  $\eta$ , in Fig. 11a, and on the TX speed,  $v^{\text{tx}}$ , in Fig. 11b. The results obtained for Setup 1 are marked by SU1.

AsyMov achieves 2.84 Hz Doppler error in Setup 1 with  $KT = 16$  ms (see Tab. 2). This result remains consistent when the number of static paths changes from  $S = 2$  to  $S = 3$ , with the same mean and spread. Moreover, we compare the estimation error with respect to a scenario with static RX and TX, showing that the error is only slightly higher using AsyMov with a moving TX. This demonstrates that our approach successfully copes with the motion of ISAC devices.

Fig. 11a and Fig. 11b show the distribution of the absolute error on the TX movement direction  $\eta$  and speed  $v^{\text{tx}}$ , by varying the observation window size. With a sufficiently long window, i.e., 16 ms or longer, AsyMov achieves median errors lower than  $15^\circ$  and 2 cm/s for  $\eta$  and  $v^{\text{tx}}$ , respectively. For Setup 1,  $\hat{\varepsilon}_{\eta}$  is affected by the difficulty in estimating the AoD of the LoS path, since the RX is located at the very edge of the field of view of the TX antenna. In the next section, we show that the more realistic Setup 2 leads to substantial improvements in the estimate of  $\eta$ .



(a) Absolute  $\eta$  estimation error. (b) Absolute  $v_{tx}$  estimation error.

Fig. 11: Varying the duration of the processing window, with  $S = 2$ .

2) *Results for Setup 2:* The bottom plot in Fig. 10 shows the target Doppler estimate for an experiment in Setup 2. The reduced strength of the reflection on the target makes the estimation more difficult than in Setup 1. This is due to the relation between the path amplitudes and the phase noise, see Eq. (21) (namely, the noise variance is inversely proportional to the squared amplitudes). This explains why at around 2 s the estimation becomes inaccurate.

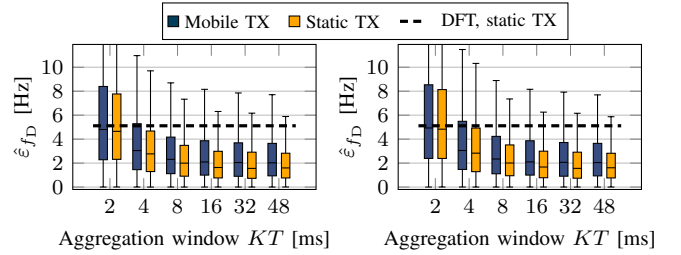
Tab. 2 reports the estimation error for  $f_{D,t}$  in Setup 2 (SU2) for either a static or mobile TX, considering an observation window of  $KT = 16$  ms. The error is larger than that in Setup 1, but on par with the static TX case (around 18 Hz). This demonstrates that AsyMov can effectively cope with the TX motion even in a more realistic bistatic scenario.

Fig. 11a and Fig. 11b show the error distribution of  $\hat{\eta}$  and  $\hat{v}^{tx}$  for Setup 2. As anticipated above, for long processing windows AsyMov achieves a lower error on  $\eta$  compared to Setup 1, being thus able to better exploit a higher number of channel estimates. This is mostly due to the more accurate AoD estimation of the LoS path angle for Setup 2, since the RX in this configuration resides in the central region of the field of view of the TX antenna. Conversely, the error on  $\hat{v}^{tx}$  is slightly higher for Setup 2. With  $KT$  larger than 16 ms, AsyMov obtains median errors for  $\hat{\eta}$  and  $\hat{v}^{tx}$  smaller than  $10^\circ$  and 3 cm/s, respectively.

#### D. Comparison to static DFT processing

In this section, we compare AsyMov to a standard method to estimate the Doppler frequency of a target, using Setup 1 as the reference scenario. This method is applied to *static* TX and RX devices and utilizes the DFT to identify the peak of the CIR corresponding to the target. The location of the peak in the Doppler frequency spectrum is thus taken as the estimate of the target Doppler. Before applying the DFT, the CFO and PO need to be removed to avoid a bias in the location of the peak. To this purpose, we multiply the target CIR peak by the complex conjugate of the LoS one, which cancels out the frequency and phase offsets (see the method in [10]). We also vary the duration of the observation window and apply AsyMov to a static TX. For the DFT baseline, we use the longest observation window from our experiments,  $KT = 48$  ms.

Fig. 12 shows the Doppler estimation error with (a)  $S = 2$  and (b)  $S = 3$  static paths. The black dashed line represents the median error of the DFT-based method. AsyMov obtains lower estimation errors even with an aggregation window of



(a)  $S = 2$  static paths. (b)  $S = 3$  static paths.

Fig. 12: Setup 1, DFT over  $KT = 48$  ms.

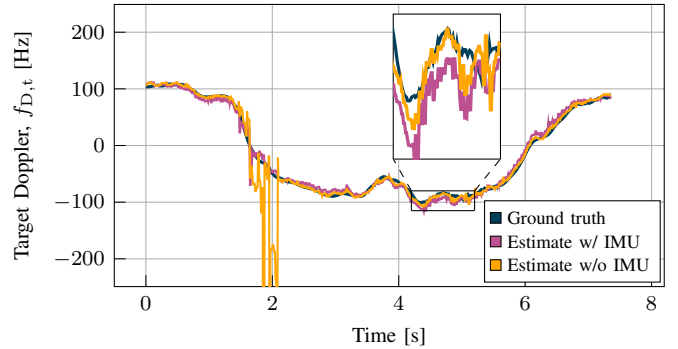


Fig. 13: Target Doppler frequency with  $S = 2$  and  $KT = 16$  ms.

2 ms, reducing by 24 times the window length with respect to the DFT approach. With AsyMov, increasing the observation window leads to an error as low as 2.3 Hz with  $S = 2$ , which is less than half the error attained by the DFT-based method. Moreover, we observe that using AsyMov with a static or moving TX yields nearly identical performance.

#### E. Integration with IMU

Finally, we test the integration of our model with the TX velocity measured by the onboard IMU sensor. This is done by obtaining an estimate of  $v^{tx}$  from the IMU, in the reference system of the TX. Then, this velocity is used as an additional input to AsyMov, thus the number of unknowns is reduced to two and the system in Eq. (18) can be solved using a single static reference path. We do not use the estimate of  $\eta$  obtained from the IMU, as we observed that it is rather unreliable and its use is likely to degrade the estimation performance.

As shown in Fig. 13, integrating the TX speed measurement from the IMU could enhance the reliability of AsyMov. In this experiment, the CIR peak corresponding to one of the required static paths is not detected for several subsequent frames in the interval  $[1.5, 2.1]$  s. Within this time interval, AsyMov lacks sufficient information (static paths) to estimate the target Doppler frequency and fails, as shown by the yellow curve. Conversely, when feeding the IMU measurement to AsyMov, the Doppler frequency is estimated accurately even when not all the CIR peaks are detected (pink curve). Interestingly, when all the required CIR peaks are available, AsyMov is more accurate *without* using the IMU measurement, hence only relying on the wireless signal. This is evident from the zoom plot in Fig. 13 and from Tab. 3, where we quantitatively evaluate the Doppler estimation error for three different time intervals in the experiment of Fig. 13. While in the interval

TABLE 3: Average target Doppler frequency estimation error  $\pm$  one standard deviation, with one undetected path within [1.5, 2.1] s.

Error [Hz]	Time interval		
	[0, 1.5] s	[1.5, 2.1] s	[2.1, 7.3] s
w/ IMU	5.32 $\pm$ 4.04	<b>10.72 <math>\pm</math> 12.32</b>	6.51 $\pm$ 3.89
w/o IMU	<b>2.06 <math>\pm</math> 2.24</b>	168 $\pm$ 518	<b>2.91 <math>\pm</math> 2.33</b>

[1.5, 2.1] s (undetected CIR path) using the IMU gives a large performance gain, outside of this interval a sufficient number of static paths is available. In this case, estimating the Doppler solely based on the wireless channel cuts the estimation error by half with respect to using the IMU.

Based on these results, the decision as to whether the onboard IMU is to be used shall be made based on the number of available (detected) static CIR paths. If such number is greater than 2 already, the IMU will not provide additional benefits, but can be exploited to compensate for the temporary lack of a sufficient number of static channel reflections.

## VII. CONCLUDING REMARKS

In this paper, we proposed AsyMov, a method to estimate the Doppler frequency of a target in an *asynchronous* ISAC system featuring *mobile* ISAC devices. Our approach effectively disentangles the target's Doppler frequency from the phase offsets due to clock asynchrony and the Doppler caused by the device movement if at least 2 static multipath components are available. By exploiting phase differences across multipath components, across time, and the multipath geometry, AsyMov casts Doppler estimation as a non-linear least-square problem that can be iteratively solved, attaining high-quality estimates for the target's Doppler frequency and the velocity of the moving ISAC device. Differently from traditional DFT-based processing, AsyMov handles channel estimates obtained at irregular time intervals. Moreover, it can be seamlessly integrated with measurements from an IMU sensor, positioned on the moving ISAC device, to provide increased robustness as some of the static paths become temporarily unavailable. AsyMov has been thoroughly assessed via theoretical analysis, numerical simulation, and experimental evaluation, showing that its performance is comparable to that achieved with static ISAC devices.

### APPENDIX A

We first observe that Eq. (15) does not contain the Doppler frequency of the target. Hence, we use it with  $s = 1$  to obtain write  $v^{\text{tx}}$  as a function of  $\eta$  (note that a similar expression is obtained using  $s = 2$ )

$$v^{\text{tx}} = \frac{\lambda \bar{\Delta}_1}{\cos(\eta - \alpha_1) - \cos \eta}. \quad (26)$$

Then, using the above result into Eq. (15) with  $s = 2$ , and solving for  $\eta$  we get

$$\tan \eta = \frac{\bar{\Delta}_2(\cos \alpha_1 - 1) - \bar{\Delta}_1(\cos \alpha_2 - 1)}{\bar{\Delta}_1 \sin \alpha_2 - \bar{\Delta}_2 \sin \alpha_1} \triangleq \xi. \quad (27)$$

Inverting the above equation as  $\hat{\eta} = \arctan \xi$  would cause an ambiguity, since the codomain of the arctan function is

$[-\pi/2, \pi/2]$ . This would exclude from the solution the (valid) cases where  $\eta \in [\pi/2, 3\pi/2]$ . To resolve the ambiguity, we start by noticing that

$$\bar{\Delta}_1 \sin \alpha_2 - \bar{\Delta}_2 \sin \alpha_1 = \frac{v^{\text{tx}}}{\lambda} u(\alpha_1, \alpha_2) \cos \eta, \quad (28)$$

where  $u(\alpha_1, \alpha_2) = \sin \alpha_1(1 - \cos \alpha_2) + \sin \alpha_2(\cos \alpha_1 - 1)$ . Eq. (28) is obtained after some manipulations by substituting the expressions of  $\bar{\Delta}_1$  and  $\bar{\Delta}_2$ . The left-hand side of Eq. (28) and  $u(\alpha_1, \alpha_2)$  can be computed numerically using the phase measurements and the AoD estimates. Hence, we have that

$$\text{sign}(\cos \eta) = \text{sign} \left( \frac{\bar{\Delta}_1 \sin \alpha_2 - \bar{\Delta}_2 \sin \alpha_1}{u(\alpha_1, \alpha_2)} \right), \quad (29)$$

since  $v^{\text{tx}}/\lambda$  is positive by definition. From the sign of  $\cos \eta$  we can understand whether  $\eta \in [-\pi/2, \pi/2]$  (if  $\cos \eta$  is positive) or  $\eta \in [\pi/2, 3\pi/2]$  (if  $\cos \eta$  is negative). This is then used to disambiguate Eq. (27) as follows

$$\hat{\eta} = \begin{cases} \arctan \xi & \text{if } \cos \eta \geq 0, \\ \pi + \arctan \xi & \text{if } \cos \eta < 0. \end{cases} \quad (30)$$

We substitute  $\hat{\eta}$  into the expression of  $v^{\hat{\text{tx}}}$ , then use  $\hat{\eta}$  and  $\hat{v}^{\text{tx}}$  into Eq. (14) to obtain Eq. (20).

### APPENDIX B

The approximated noise variance on the phase of path  $i$  can be obtained following [39]

$$\sigma_{\phi,i}^2 = \left( \frac{\partial \mathcal{L} h_i[k, l_i]}{\partial \Re\{h_i\}} \right)^2 \frac{\sigma_h^2}{2} + \left( \frac{\partial \mathcal{L} h_i[k, l_i]}{\partial \Im\{h_i\}} \right)^2 \frac{\sigma_h^2}{2} \quad (31)$$

$$= \frac{\sigma_h^2}{2|A_i|^2} = \frac{\sigma_w^2}{2G|A_i|^2}. \quad (32)$$

Eq. (32) states that the noise variance on the phase of a path is inversely proportional to the squared magnitude of that path.

### APPENDIX C

Defining the following auxiliary variables

$$\rho_i = \sin(\alpha_i - \eta) + \sin(\eta), \quad i \in \{t, 1, 2\}, \quad (33)$$

$$\gamma_i = \cos(\alpha_i - \eta) - \cos(\eta), \quad i \in \{t, 1, 2\} \quad (34)$$

and plugging into Eq. (32), the elements of the FIM are

$$\mathbf{J}_{1,1} = \frac{4\pi^2 G T_k^2}{\sigma_w^2 \kappa_t}, \quad \mathbf{J}_{1,2} = \frac{4\pi^2 G T_k^2 v^{\text{tx}}}{\lambda \sigma_w^2 \kappa_t} \rho_t, \quad (35)$$

$$\mathbf{J}_{1,3} = \frac{4\pi^2 G T_k^2}{\lambda \sigma_w^2 \kappa_t} \gamma_t, \quad \mathbf{J}_{2,2} = \frac{4\pi^2 G T_k (v^{\text{tx}})^2}{\lambda^2 \sigma_w^2} \sum_i \frac{\rho_i^2}{\kappa_i}, \quad (36)$$

$$\mathbf{J}_{2,3} = \frac{4\pi^2 G T_k v^{\text{tx}}}{\lambda^2 \sigma_w^2} \sum_i \frac{\rho_i \gamma_i}{\kappa_i}, \quad \mathbf{J}_{3,3} = \frac{4\pi^2 G T_k}{\lambda^2 \sigma_w^2} \sum_i \frac{\gamma_i^2}{\kappa_i}, \quad (37)$$

where the index in the summations is intended as  $i \in \{t, 1, 2\}$ .

Inverting the FIM, we obtain matrix  $\mathbf{J}^{-1}$ , that contains the CRLB values for each parameter in  $\theta$  on its diagonal. The final CRLB for the target Doppler frequency is given by Eq. (24), where the term  $\zeta_{t,1,2}$  is given in Eq. (38).

$$\begin{aligned}
\zeta_{t,1,2} = & 3(\kappa_1 + \kappa_2 + \kappa_t) - (\kappa_2 + \kappa_t)(2\cos\alpha_1 + \cos(2\alpha_1)) + 2\kappa_t(\cos(\alpha_1 - 2\alpha_2) + \cos(\alpha_1 - \alpha_2)) - \kappa_t\cos(2(\alpha_1 - \alpha_2)) \\
& + 2\kappa_t\cos(2\alpha_1 - \alpha_2) - (2\kappa_1 + \kappa_t)(2\cos(\alpha_2)\cos(2\alpha_2)) + 2\kappa_t\cos(\alpha_1 + \alpha_2) - 2\kappa_2\cos(\alpha_1 - 2\alpha_t) + 2\kappa_1\cos(\alpha_2 - 2\alpha_t) \\
& - 2\kappa_2\cos(\alpha_1 - \alpha_t) - \kappa_2\cos(2(\alpha_1 - \alpha_t)) + 2\kappa_2\cos(2\alpha_1 - \alpha_t) + 2\kappa_1\cos(2\alpha_2 - \alpha_t) - (2\kappa_1 + 2\kappa_2)\cos(\alpha_t) \\
& - (\kappa_1 + \kappa_2)\cos(2\alpha_t) + 2\kappa_2\cos(\alpha_1 + \alpha_t) + 2\kappa_1\cos(\alpha_2 + \alpha_t)
\end{aligned} \tag{38}$$

## REFERENCES

- [1] F. Liu *et al.*, “Seventy years of radar and communications: The road from separation to integration,” *IEEE Signal Process. Mag.*, vol. 40, no. 5, pp. 106–121, 2023.
- [2] M. A. Richards, J. Scheer, W. A. Holm, and W. L. Melvin, *Principles of modern radar*. Raleigh, NC, USA: Scitech Publishing Inc., 2010.
- [3] B. Vandersmissen *et al.*, “Indoor person identification using a low-power FMCW radar,” *IEEE Trans. Geosci. Remote Sens.*, vol. 56, no. 7, pp. 3941–3952, 2018.
- [4] Y. Chu, K. Cumanan, S. K. Sankarpani, S. Smith, and O. A. Dobre, “Deep Learning-Based Fall Detection Using WiFi Channel State Information,” *IEEE Access*, vol. 11, pp. 83 763–83 780, 2023.
- [5] X. Fang and G. Xiao, “Rotor Blades Micro-Doppler Feature Analysis and Extraction of Small Unmanned Rotorcraft,” *IEEE Sensors J.*, vol. 21, no. 3, pp. 3592–3601, 2021.
- [6] J. A. Zhang *et al.*, “Enabling joint communication and radar sensing in mobile networks—a survey,” *IEEE Commun. Surveys Tuts.*, vol. 24, no. 1, pp. 306–345, 2021.
- [7] A. Singh, S. U. Rehman, S. Yongchareon, and P. H. J. Chong, “Multi-Resident Non-Contact Vital Sign Monitoring Using Radar: A Review,” *IEEE Sensors J.*, vol. 21, no. 4, pp. 4061–4084, 2021.
- [8] J. A. Zhang, K. Wu, X. Huang, Y. J. Guo, D. Zhang, and R. W. Heath, “Integration of radar sensing into communications with asynchronous transceivers,” *IEEE Commun. Mag.*, vol. 60, no. 11, pp. 106–112, 2022.
- [9] K. Wu *et al.*, “Sensing in Bistatic ISAC Systems With Clock Asynchronism: A signal processing perspective,” *IEEE Signal Process. Mag.*, vol. 41, no. 5, pp. 31–43, 2024.
- [10] J. Pegoraro *et al.*, “JUMP: Joint Communication and Sensing With Unsynchronized Transceivers Made Practical,” *IEEE Trans. Wireless Commun.*, vol. 23, no. 8, pp. 9759–9775, 2024.
- [11] F. Meneghello, D. Garlisi, N. Dal Fabbro, I. Tinnirello, and M. Rossi, “SHARP: Environment and Person Independent Activity Recognition with Commodity IEEE 802.11 Access Points,” *IEEE Trans. Mobile Comput.*, vol. 22, no. 10, pp. 6160–6175, 2023.
- [12] F. Zhang, J. Xiong, Z. Chang, J. Ma, and D. Zhang, “Mobi2Sense: empowering wireless sensing with mobility,” in *Proc. of the 28th Annual Int. Conf. on Mobile Computing And Networking*, ser. MobiCom ’22. New York, NY, USA: ACM, 2022, p. 268–281.
- [13] Z. Chang, F. Zhang, J. Xiong, W. Chen, and D. Zhang, “MSense: Boosting Wireless Sensing Capability Under Motion Interference,” in *Proc. of the 30th Annual Int. Conf. on Mobile Computing and Networking*, ser. ACM MobiCom ’24. New York, NY, USA: ACM, 2024, p. 108–123.
- [14] J. Liu *et al.*, “Towards a Dynamic Fresnel Zone Model to WiFi-based Human Activity Recognition,” *Proc. ACM Interact. Mob. Wearable Ubiquitous Technol.*, vol. 7, no. 2, Jun. 2023.
- [15] J. Zhao, Z. Lu, J. A. Zhang, S. Dong, and S. Zhou, “Multiple-Target Doppler Frequency Estimation in ISAC with Clock Asynchronism,” *IEEE Trans. Veh. Technol.*, vol. 73, no. 1, pp. 1382–1387, 2024.
- [16] A. Garcia-Rodriguez, D. López-Pérez, L. Galati-Giordano, and G. Geraci, “IEEE 802.11be: Wi-Fi 7 Strikes Back,” *IEEE Commun. Mag.*, vol. 59, no. 4, pp. 102–108, 2021.
- [17] J. Pegoraro, J. O. Lacruz, M. Rossi, and J. Widmer, “SPARCS: A Sparse Recovery Approach for Integrated Communication and Human Sensing in mmWave Systems,” in *21st ACM/IEEE Int. Conf. on Information Processing in Sensor Networks (IPSN)*, Milan, Italy, May 2022.
- [18] C. B. Barneto, S. D. Liyanaarachchi, M. Heino, T. Riihonen, and M. Valkama, “Full Duplex Radio/Radar Technology: The Enabler for Advanced Joint Communication and Sensing,” *IEEE Wireless Commun.*, vol. 28, no. 1, pp. 82–88, 2021.
- [19] M. Heino, C. B. Barneto, T. Riihonen, and M. Valkama, “Design of Phased Array Architectures for Full-Duplex Joint Communications and Sensing,” in *2021 15th European Conf. on Antennas and Propagation (EuCAP)*. IEEE, 2021, pp. 1–5.
- [20] J. Pegoraro, J. O. Lacruz, F. Meneghello, E. Bashirov, M. Rossi, and J. Widmer, “RAPID: Retrofitting IEEE 802.11ay Access Points for Indoor Human Detection and Sensing,” *IEEE Trans. Mobile Comput.*, vol. 23, no. 5, pp. 4501–4519, 2024.
- [21] O. Kanhere, S. Goyal, M. Beluri, and T. S. Rappaport, “Target Localization using Bistatic and Multistatic Radar with 5G NR Waveform,” in *2021 IEEE 93rd Vehicular Technology Conf. (VTC)*, 2021, pp. 1–7.
- [22] L. Pucci, E. Matricardi, E. Paolini, W. Xu, and A. Giorgetti, “Performance Analysis of a Bistatic Joint Sensing and Communication System,” in *2022 IEEE Int. Conf. on Communications Workshops (ICC Workshops)*, 2022, pp. 73–78.
- [23] Z. Gao *et al.*, “Integrated Sensing and Communication With mmWave Massive MIMO: A Compressed Sampling Perspective,” *IEEE Trans. Wireless Commun.*, vol. 22, no. 3, pp. 1745–1762, 2023.
- [24] Z. Ni, J. A. Zhang, X. Huang, K. Yang, and J. Yuan, “Uplink Sensing in Perceptive Mobile Networks With Asynchronous Transceivers,” *IEEE Trans. Signal Process.*, vol. 69, pp. 1287–1300, 2021.
- [25] X. Li, J. A. Zhang, K. Wu, Y. Cui, and X. Jing, “CSI-Ratio-Based Doppler Frequency Estimation in Integrated Sensing and Communications,” *IEEE Sensors J.*, vol. 22, no. 21, pp. 20 886–20 895, 2022.
- [26] F. Zhang *et al.*, “Exploring LoRa for Long-range Through-wall Sensing,” *Proc. of the ACM on Interactive, Mobile, Wearable and Ubiquitous Technologies*, vol. 4, no. 2, pp. 1–27, 2020.
- [27] Y. Zeng, D. Wu, J. Xiong, J. Liu, Z. Liu, and D. Zhang, “MultiSense: Enabling Multi-person Respiration Sensing with Commodity WiFi,” *Proc. of the ACM on Interactive, Mobile, Wearable and Ubiquitous Technologies*, vol. 4, no. 3, pp. 1–29, 2020.
- [28] P. Yu, D. Ma, Q. Zhang, and Z. Feng, “Efficient Clock Offset Calibration Method for Uplink Sensing in Asynchronous ISAC System,” in *2024 2nd Int. Conf. On Mobile Internet, Cloud Computing and Information Security (MICCIS)*, 2024, pp. 43–47.
- [29] G. Ventura, Z. Bhalli, M. Rossi, and J. Pegoraro, “Bistatic Doppler Frequency Estimation With Asynchronous Moving Devices for Integrated Sensing and Communications,” *IEEE Wireless Commun. Lett.*, vol. 13, no. 10, pp. 2872–2876, 2024.
- [30] J. A. Zhang *et al.*, “An overview of signal processing techniques for joint communication and radar sensing,” *IEEE J. Sel. Topics Signal Process.*, vol. 15, no. 6, pp. 1295–1315, 2021.
- [31] N. J. Willis, *Bistatic radar*. SciTech Publishing, 2005, vol. 2.
- [32] D. Garcia, J. O. Lacruz, P. J. Mateo, J. Palacios, R. Ruiz, and J. Widmer, “Scalable Phase-Coherent Beam-Training for Dense Millimeter-Wave Networks,” *IEEE Trans. Mobile Comput.*, vol. 22, no. 4, pp. 2353–2369, 2023.
- [33] J. Nocedal and S. Wright, *Numerical optimization*. Springer Science & Business Media, 2006.
- [34] S. M. Kay, “Statistical signal processing: estimation theory,” *Prentice Hall*, vol. 1, pp. Chapter–3, 1993.
- [35] 3GPP, “Technical Specification Group Radio Access Network; User Equipment (UE) radio transmission and reception; Part 2: Range 2 Standalone (Release 16),” *3rd Generation Partnership Project (3GPP), techreport TR 38.101-2*, Mar. 2020, version 16.3.0.
- [36] J. O. Lacruz, R. R. Ortiz, and J. Widmer, “A Real-Time Experimentation Platform for sub-6 GHz and Millimeter-Wave MIMO Systems,” in *Proc. of the 19th Annual Int. Conf. on Mobile Systems, Applications, and Services*, ser. MobiSys ’21. New York, NY, USA: ACM, 2021, p. 427–439.
- [37] IEEE 802.11 working group, “IEEE Draft Standard for Information Technology-Telecommunications and Information Exchange Between Systems Local and Metropolitan Area Networks-Specific Requirements Part 11: Wireless LAN MAC and PHY Specifications-Amendment: Enhanced Throughput for Operation in License-Exempt Bands Above 45 GHz,” *IEEE P802.11ay/D3.0*, 2019.
- [38] C.-Y. Liu *et al.*, “Dual-Mode All-Digital Baseband Receiver With a Feed-Forward and Shared-Memory Architecture for Dual-Standard Over 60 GHz NLOS Channel,” *IEEE Trans. Circuits Syst.*, vol. 64, no. 3, pp. 608–618, 2017.
- [39] H. H. Ku, “Notes on the use of propagation of error formulas,” *Journal of Research of the National Bureau of Standards*, vol. 70, no. 4, pp. 263–273, 1966.